On the Application of a Damped Model to the Falling Weight Impact Characterization of Glass Beads–Polystyrene Composites

M. Sánchez-Soto, A. B. Martínez, O. O. Santana, A. Gordillo

Centre Català del Plàstic, Universitat Politécnica de Catalunya, C/Colom 114, 08222 Terrassa, Spain

ABSTRACT: Instrumented falling weight impact tests were carried out to characterize the mechanical behavior of a material pattern formed by polystyrene and different amounts of glass beads. This characterization was performed at high strain rate using two different impact arrangements: the first uses high impact energy at the striker, whereas the second uses a low-impact energy. Starting from a conservative model, a nonconservative one has been proposed for the low-energy impact configuration as a better approach to the material behavior. In this latter model, the energy losses were quantified through the restitution coefficient. Two alternative methods for its calculation are described. The results shows good agreement between the flexural modulus and break stresses calculated in either the low- or the high-energy arrangement; however, the low-energy impact method yields more confidence results. Using the proposed model, the composites' fracture onset was determined, and also in the samples with low content of glass beads, it was possible to assess the micromechanism of failure, given the estimation for the stress to produce crazing. © 2004 Wiley Periodicals, Inc. J Appl Polym Sci 93: 1271–1284, 2004

Key words: impact resistance; fracture; modeling; mechanical properties; crazing

INTRODUCTION

The high-speed impact between two bodies is a matter of great importance because many important material parameters have to be determined under this condition. One of the methods used to study the impact behavior of a solid component is the instrumented falling weight impact (IFWI). In this test, a mass is dropped from a determined height to have an impact on the sample with the aim of measuring its mechanical response. The striker is instrumented with a load sensor located very close to the impact point, so it is possible to obtain a complete record of the impact event, extracting force–time or force–displacement evolutions. From this record some of the sample mechanical properties, such as the Young's modulus, the load at break, or the material fracture parameters, can be obtained.[1–3]

The falling weight testing has been steadily acquiring importance in the high-speed description of polymers because it has the advantage of multiaxiality and the possibility of working with finished articles.[5–9] In the most generalized procedure the dart energy must be in excess to ensure that specimen fracture occurs without a significant loss in the dart velocity.[1] However, one of the main problems, especially when dealing with brittle materials, is the presence of dynamics effects. These effects are a consequence of the propagation of stress waves in the material under test or caused by the acceleration imparted to the specimen that makes the sample vibrate, yielding successive contacts between striker and sample.[2,4] At high strain rates the oscillation amplitudes can be even higher than the load peak, and the force acting over the sample could be rather different from that measured in the headstock. Under this circumstances the analysis of the experimental curve becomes very difficult.

The low-energy impact testing traditionally was used to determine the incident energy at which 50% of the impacted specimens fail. Originally the procedure was statistical, giving no quantitative information about the energy for fracture initiation or about the material mechanical behavior. Nowadays, the development of electronic instrumentation has overcome these inconveniences and the technique could be used to investigate situations like when internal damage is created by a soft impact. The main advantage of the low-energy impact configuration is the minimization of dynamics effects, obtaining force–time curves without oscillations.[10] In addition the damage caused in the specimen could be modified by introducing a

slight variation in the striker energy. As a result, the material characterization is easily performed.

The methods applied to predict the force–time evolution in a low-energy impact are, in general, derived from a simple spring–mass model.[11] This approach considers the material perfectly elastic and to behave in a conservative way. When working in high-energy conditions the energy losses are negligible with respect to the falling one; however, in low-energy arrangements these losses cannot be ignored. On the other hand, all materials are nonconservative to some degree, so an approach to its experimental behavior needs to include the inelasticity phenomenon.

To verify the application feasibility of the low-energy impact method, a material pattern composed of polystyrene (PS) and different amounts of solid glass beads (GB) was used. Polystyrene is an amorphous glassy thermoplastic where crazing is the dominant deformation mechanism. Glass beads are preferred as filler material, especially when properties like isotropy are desirable. Compared with other fillers, glass beads have only a minor contribution in the increment of melt viscosity, thus providing an easy transformation, and then the orientation events associated with molding are minimal. As a result, polystyrene–glass beads composites will be, in advance, uniformly reinforced systems characterized by a quasi–lineal-elastic behavior and with a well-defined deformation micromechanism.[12–15] Further, the matrix transparency favors the identification of the damage occasioned by the impact, making it possible to follow the damage evolution as a function of the glass bead content.

One of the objectives of this work was to assess for the viability of low-energy falling weight impact technique to characterize plastic materials and composites. Starting from the conservative model, an easy nonconservative dashpot–spring model with analytical solution is proposed as a better approximation to the low-energy shock behavior. Another objective was to take into account the energy impact losses by incorporating the restitution coefficient into the model. In this sense, a direct process to determine this coefficient is proposed. Finally, the impact behavior of net polystyrene and polystyrene glass bead composites is compared by the two referred testing methods: high-energy impact testing and low-energy impact testing.

EXPERIMENTAL

Materials and specimen preparation

The polystyrene used in the experiments was a Lacqrene 1541 grade, supplied by AtoFina-Elf (Paris, France). This polystyrene was of injection type and had a high fluidity, showing a melt flow index of 12 g/10 min at 200°C and 5 kg. The PS was mixed with a second phase of glass beads (GB) to form seven PS–GB

TABLE I
Glass Bead Content and Poisson Coefficient for PS and PS–GB Composites[a]

Sample	GB content (% w)	Poisson coefficient
GB	100	0.230
PS	0	0.320
PS–GB2	1.91 ± 0.02	0.319
PS–GB6	6.25 ± 0.17	0.318
PS–GB10	10.16 ± 0.03	0.316
PS–GB15	14.78 ± 0.14	0.314
PS–GB25	25.38 ± 0.07	0.308
PS–GB40	40.16 ± 0.51	0.299

[a] Poisson coefficient was obtained applying the rule of mixtures.

composites with beads content ranging from 0 to 40% in weight. The glass beads were supplied by Sovitec Ibérica SA (Castellbisbal, Spain), having an average particle size of 27.4 μm and a size distribution varying between 2 and 120 μm. In all cases the beads used were nonsuperficially treated. The main characteristics and the nomenclature used for the composites are shown in Table I.

To obtain homogeneous particle dispersion the components were blended in a corotating twin-screw extruder Collin T20 (Ebersberg, Germany) with length to diameter ratio of 24. The temperature profile from hopper to die was 70, 120, 145, 160, and 165°C. These temperatures were selected in the low material range to avoid degradation. On the other hand, the low viscosity of the selected PS matrix allowed preparation of the composites without the application of higher shear levels. Once obtained, the extruded material was cooled with water and chopped before being injected. The injection unit was a Mateu and Solé (Barcelona, Spain) Meteor 440/90 of 90 ton clamping force. Edge-gated disc specimens (diameter 80 mm; 4 mm thick) were molded. Temperature at the die was 230°C and the mold temperature was set to 60°C. Samples were finally tempered at 85°C for 6 h to relax internal stresses.

Impact testing equipment and procedure

Falling weight tests were performed with a Ceast Dartvis (Torino, Italy) instrumented impact equipment. The dart had a hemispherically shaped headstock (diameter 12.7 mm) instrumented by extensometric gauges with an acquiring frequency of 125 kHz. The impact energy of the device was modified either by a change in the drop height or in the total mass of the dart.

Selection of the proper impact velocity was performed along with the dropped mass with the intention of obtaining smooth impact curves. For the low-

energy impacts a dropping mass of 0.712 kg and a speed range between 0.5 and 1.7 m/s were chosen. For high-energy impacts the total falling mass was of 3.743 kg and the speed was constant at 0.82 m/s. According to Johnson[16] in the selected range of impact speeds the heating effects are negligible because the used velocities are extremely remote from the threshold one.

In all the studied cases the samples were simply supported on an annular ring with inner and outer diameters of 60 and 80 mm, respectively. The tests were performed at room temperature.

Impact velocity calibration

The impact speed just before collision (v_0) could be calculated in two different ways. The first method is simply derived from the drop height (h); in this case the impact speed (v_{0h}) is obtained from

$$V_{0h} = \sqrt{2gh} \tag{1}$$

where g represents the gravity acceleration. In the second method, the impact-measured speed (v_{0m}) is found when a small flag placed at the striker crosses a photoelectric cell located close to the impact point. The first methodology does not take into account the losses caused by friction, whereas the second one is not very accurate if very low height drops (<13 mm) are used.

To adjust the impact speed values (v_0), the dart was dropped from different heights, between 15 and 110 mm, with height increments of 5 mm. The velocities v_{0h} and v_{0m} were then determined and compared.

In the high-energy impact conditions, it was not necessary to apply velocity correction because in this configuration the velocity is detected by the photoelectric cell and all the possible velocities losses are incorporated through integration of the force–time record. However, several replicas were performed over each sample to ensure the constancy of the impact force.

Microscopy

Observations of impacted specimens were made using optic and electronic microscopy. A reflection optical microscope (Carlton) was used, particularly with highly filled composites, to observe superficial damage near the impacted area. A Nikon-Optiphot Pol (Nikon, Tokyo, Japan) transmitted light polarizing microscope was used mainly in clear or translucent samples, that is, in samples filled up to 10% wt of glass beads. All observations were carried out just after the collision was produced. Scanning electron microscopy was performed on fracture disc surfaces using a JSM 6400 microscope (JEOL, Tokyo, Japan). Before observation, specimens were vacuum coated with a thin layer of gold to make them electrically conductive.

MODEL DESCRIPTION

High-impact energy testing

If the impact conditions are such that the dart fully penetrates the discs without a significant velocity change (<20%), the energy lost by the dart is negligible and a quasi-static analysis could be applied to characterize the materials. The equations that yield the absorbed energy and dart displacement as time functions can be found elsewhere.[1] Once the evolution of this set of variables is obtained, the equipment software allows crossing them to obtain the more useful force–displacement or energy–displacement curves.

The materials parameters are found by applying the equation for deflection of simply supported circular plates of constant thickness,[20] and the Young's modulus is obtained through

$$E = \frac{6(3 + v)(1 - v)r^2}{8\pi h^3} \frac{F}{\alpha} \tag{2}$$

where v is the material Poisson coefficient, r is the specimen radius, h is the sample thickness, and F/α is the slope of the force–displacement curve or the flexural specimen compliance. The material failure strength is obtained from the maximum stress value, expressed by

$$\sigma_m = \frac{F_m}{h^2}\left[(1 + v)\left(0.485 \log \frac{r}{h} + 0.52\right) + 0.48\right] \tag{3}$$

where F_m is the maximum recorded force during the impact event.

Low-impact energy testing

Restitution coefficient

The restitution coefficient (ε) is an empirical parameter used to treat the loss of energy on impact. It is defined as the ratio between the approach velocity and the velocity after the collision. The coefficient always has a positive value, for which the limits are one for a pure elastic contact and zero for a pure inelastic contact.[17] This coefficient allows quantifying the inelasticity of the tested specimens during the impact event.

If we take v_0 as the striker velocity just before the collision and v_1 as the velocity just after contact, the restitution coefficient is defined by

$$\varepsilon = \frac{v_1}{v_0} \tag{4}$$

The restitution coefficient can be calculated in two different ways. In the first procedure the value of v_0 is known from the drop height or from direct measurement by use of, in this case, a photoelectric cell. The v_1

(a)

(b)
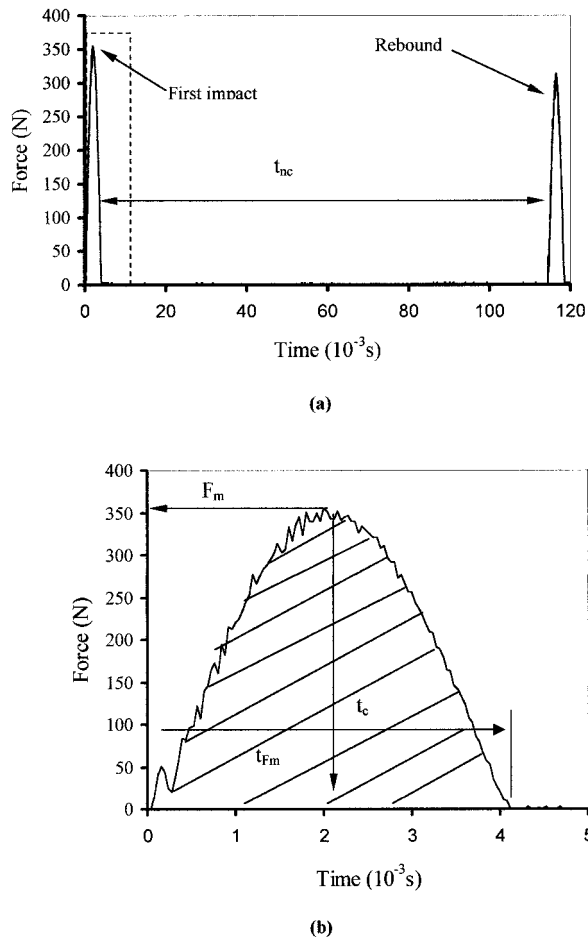
Figure 1   (a) Global force–time trace of an impact followed by a rebound event over polystyrene at 20 mm height; t_{nc} represents the noncontact time. (b) Amplification of the first contact between headstock and sample [dotted zone of (a)]. The dashed area represents the integral $\int F\,dt$ term. Key: F_m, maximum force; t_{F_m} time of maximum force; t_c, contact time.

value can be obtained if we allow the striker to have a second contact, or a rebound, with the sample [Fig. 1(a)]. The equation of the velocity after the impact event is given by

$$v_1 = \frac{g}{2} t_{nc} \qquad (5)$$

where t_{nc} is the noncontact time. The noncontact time is the time gap between the end of the first impact and the beginning of the second impact in a rebound essay. It is shown in Figure 1(a). The contact time (t_c) is defined as the period where headstock and sample are in physical touch. The second way to determine the restitution coefficient is equating impulse and momentum, as follows:

$$\int_{v_0}^{v_1} mv = \int_0^{t_c} F\,dt \qquad (6)$$

In the above equation m is the mass, v is the velocity, and F is the force recorded by the load gauges. The integration yields

$$mv_0(1 + \varepsilon) = \int_0^{t_c} F\,dt \qquad (7)$$

and

$$\varepsilon = \frac{\displaystyle\int_0^{t_c} F\,dt}{mv_0} - 1 \qquad (8)$$

The upper term of the preceding expression can be easily calculated by numerical integration of the experimental recorded force–time curve. An example is shown in Figure 1(b), where the dashed area represents the integral term. In this work this last procedure was preferred to calculate ϵ, although both methods provide the same values.

Conservative model

The collision between a rigid hemispherical element and the specimen [Fig. 2(a)] can be represented by a mass–spring model.[18] In this model the specimen is replaced by a lineal spring of constant K, where K is the static force to produce a unitary deflection on it. The specimen mass is normally negligible, and then the model can be simplified, as shown in Figure 2(b). In this case, m represents the equivalent or total system mass, which, in turn, is the falling mass.

The constant K is a function of the particular impact test geometry. In the case of the elastic deflection of a circular simple supported disc centrally loaded, the flexural rigidity is obtained from[19,20]

$$K = \frac{F}{\alpha} = \frac{16\pi(1 + v)D}{(3 + v)r^2} = \frac{4\pi Ee^3}{3(3 + v)(1 - v)r^2} \qquad (9)$$

where F is the applied force, α is the sample displacement, e is the sample thickness, r is the radius of the support, D is the disc flexural rigidity, v is the Poisson coefficient, and E is the Young's modulus.

In the conservative model the predicted force versus time evolution has a semisinusoidal shape.[21] The maximum force (F_m) depends on the total impact energy and the time in contact (t_c) on the striker mass. Both terms are also a function of the sample flexural compliance. An increment of the striker mass will simultaneously increase the maximum force level and the contact time between sample and striker. On the other hand, an increase in the drop height will promote higher velocities and impact forces, although the con-
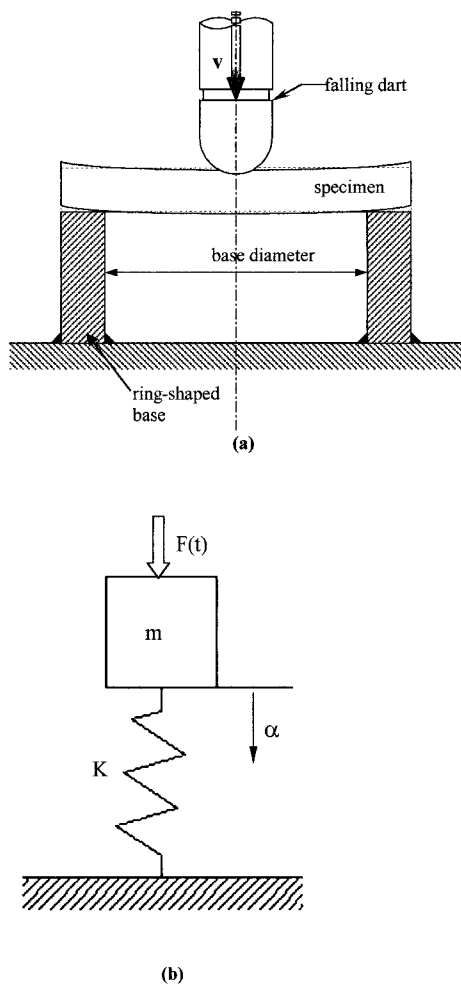
Figure 2 (a) Sketch of the impact configuration; (b) equivalent conservative model.

tact time will remain constant. The model is conservative; thus, the energy losses created during the impact event are supposed to be negligible. Further, a perfectly elastic contact between striker and sample, and a linear elastic material behavior are assumed.

The experimental application of the conservative model to the impact characterization of polymers diverges from the theoretical prediction. The higher the inelastic sample behavior, the higher the divergence. At the investigated impact velocities some of the energy dissipation sources, such as the propagation of stress waves[22] or heating effects, could be missed because only a very small portion of the kinetic energy is dissipated through these phenomena.

Nonconservative series model

With the aim of considering the energy losses produced during the impact event, a dashpot placed in series was introduced into the conservative model. The advantage of this kind of model consists in its simplicity and in the fact that it has an analytical solution; moreover, the model could be applied to different geometries only by a change in the equivalent sample compliance.

The series model is represented schematically in Figure 3. The differential equation that describes the system motion is

$$F = m\ddot{\alpha} = K\alpha_1 = C\alpha_2 \tag{10}$$

with the boundary condition

$$\alpha = \alpha_1 + \alpha_2 \tag{11}$$

where α, α_1, and α_2 are the global, spring, and dashpot displacements, respectively; and C is the dashpot constant. If the boundary conditions are applied, the solution for the displacement is expressed as

$$\alpha = \frac{v_0}{w_n}\left[2\zeta + e^{-\zeta w_n t}\left(\frac{1 - 2\zeta^2}{\sqrt{1 - \zeta^2}}\sin w_d t - 2\zeta \cos w_d t\right)\right] \tag{12}$$

and the velocity takes the form

$$\dot{\alpha} = v_0 e^{-\zeta w_n t}\left(\frac{\zeta}{\sqrt{1 - \zeta^2}}\sin w_d t + \cos w_d t\right) \tag{13}$$

Finally, the system acceleration is given by

$$\ddot{\alpha} = w_n v_0 e^{-\zeta w_n t}\left(\frac{1}{\sqrt{1 - \zeta^2}}\sin w_d t\right) \tag{14}$$

where v_0 is the drop velocity, w_n is the natural frequency, ζ is the damping coefficient, and w_d is the angular frequency, which express the system attenu-
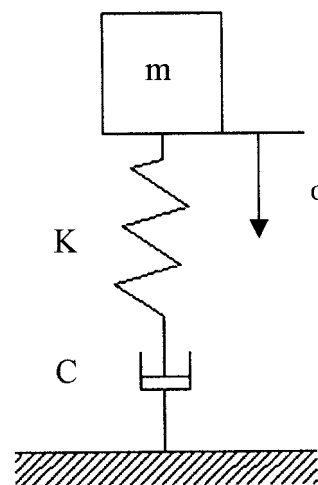

Figure 3 Nonconservative series model.

ation caused by the dashpot. The two latter terms are defined by the following expressions:

$$\zeta = \frac{\sqrt{Km}}{2C} \qquad (15)$$

and

$$w_d = w_n \sqrt{1 - \zeta^2} \qquad (16)$$

Results from this expression are useful for obtaining an explicit expression for the restitution coefficient. From eq. (14) the exerted force could be expressed as

$$F = mw_n v_0 e^{-\zeta w_n t} \frac{1}{\sqrt{1 - \zeta^2}} \sin w_d t \qquad (17)$$

The force is null at the initial moment, $t = 0$, and also at the final time step when the contact is finished. At this moment $t = t_c$ and by designating $\dot{\alpha} = v_1$, we arrive at the expression

$$v_1 = v_0 e^{-\zeta w_n t_c} \left(\frac{\zeta}{\sqrt{1 - \zeta^2}} \sin w_d t_c + \cos w_d t_c \right) \quad (18)$$

If we consider the representation of Figure 1(b), we can set the angular frequency w_d to

$$w_d = \frac{\pi}{t_c} \qquad (19)$$

and by replacing this value in eq. (18), we obtain

$$v_1 = v_0 e^{-\zeta w_n t_c} \qquad (20)$$

Then the restitution coefficient for this model is expressed by

$$\varepsilon = \frac{v_1}{v_0} = e^{-\zeta w_n t_c} = e^{-\zeta \pi / \sqrt{1 - \zeta^2}} \qquad (21)$$

Finally, it is interesting to obtain an expression that directly expresses the maximum force developed during the contact. It is clear that at maximum force level there is an inflection in the force–time curve, so

$$\frac{dF}{dt} = 0 \qquad (22)$$

By solving eq. (17) for the above condition we obtain an expression for the time at which maximum force level is reached (t_{F_m}):

$$t_{F_m} = \frac{\arctan\left(\frac{\sqrt{1 - \zeta^2}}{\zeta}\right)}{w_d} \qquad (23)$$

The expression for the maximum registered force is

$$F_m = mv_0 w_n e^{-\zeta w_n t_{F_m}} \left(\frac{1}{\sqrt{1 - \zeta^2}} \sin w_d t_{F_m} \right) \qquad (24)$$

By use of the restitution coefficient [eq. (21)], we can rearrange this equation into a more useful one:

$$F_m = mv_0 w_n \varepsilon^{t_{F_m}/t_c} \left(\frac{1}{\sqrt{1 - \zeta^2}} \sin w_d t_{F_m} \right) \qquad (25)$$

The above expression can be broken into three factors: (1) the term $mv_0 w_n$ represents the equivalent force value in the mass–spring model; (2) the exponential term of the restitution coefficient, and (3) an attenuation term (in parentheses).

RESULTS AND DISCUSSION

Composite microstructures

The morphology and orientation of the PS–GB composites can be affected by the particular injection-molding conditions and mold characteristics. It is well known that the elongation and shear flow developed in the cavity during the specimen injection molding can alter both filler structuring and matrix morphology.[23] In this sense, the anisotropy of edge-gated discs, similar to those used here, has been recently studied for polypropylene filled with aluminum and magnesium hydroxide.[24,25] The anisotropy was caused by the gate position and results in a skin–core structure, where the platy filler particles were mainly orientated in parallel to the disc surface in the skin zone. Further, different orientations of the polymer crystals were found.

In the case of the PS–GB injected discs, the anisotropy was intended to be reduced first, using small spherical glass beads as filler and, in the second term, avoiding crystallization differences by the use of an amorphous matrix. Particular care was taken to optimize and maintain similar injection-molding conditions for all the composites. In spite of these cautions, some molecular orientation could remain even after sample tempering. To qualitatively analyze the possible anisotropy, microscopic observations of the disc central surfaces were performed.

The composite microstructures obtained after injection molding are shown in Figure 4. For all compositions it can be appreciated that particles are randomly distributed over the whole fracture surface, showing no sign of agglomeration, even in the most highly
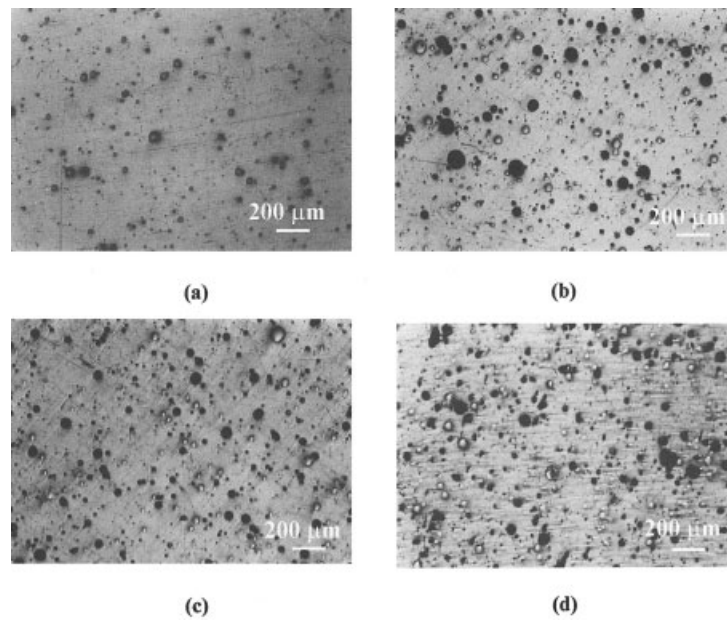
Figure 4 Particle distribution at middle center of disc samples (shaded zone) for some of the studied composites. Melt flow is perpendicular to the page. Microphotographs taken after polishing. Arrow indicates observation direction:
(a) PS–GB6;
(b) PS–GB10;
(c) PS–GB25;
(d) PS–GB40.
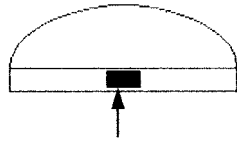
filled samples. Neither of the particle-depletion zones was observed. Assessment of the achieved particle distribution indicated that the mechanical sample property would not be influenced by particle dispersion. There is a lack of adhesion between matrix and particles, as can be deduced from the clean surface of visible beads and also from the holes left by beads that are pulled away from the matrix. Because beads are nonsuperficially treated, the only particle–matrix coupling force arises from the different shrinkage of both phases during the injection cooling. The coefficient of thermal expansion of PS (α_m) is about $8 \times 10^{-5}/°C$, whereas the coefficient for glass beads (α_b) is $8.5 \times 10^{-6}/°C$. Because $\alpha_m > \alpha_b$ the beads are initially in a state of compression.

Velocity calibration

The values relating v_{0m} and v_{0h} velocities are shown in Figure 5. The hollow graph circles represent the middle values of several investigations, making a total of 410 determinations. The best adjustment for v_0 is expressed by the following equation:

$$v_0 = 0.9686 \sqrt{2gh} \qquad (26)$$

The differences between measured and theoretical velocities are greater at very low drop height, where frictional losses are relatively important, and also the

measurement has a lack of precision. For these reasons, impacts from heights < 13 mm were discarded. If the drop height is increased, the contribution of the frictional forces with respect to the drop energy is significantly reduced.

High-energy impact testing

In all cases the application of high-energy impacts to the PS–GB composites causes the samples to break up. Under the selected testing conditions ($v = 0.82$ m/s) the loss in the impact speed was never greater than
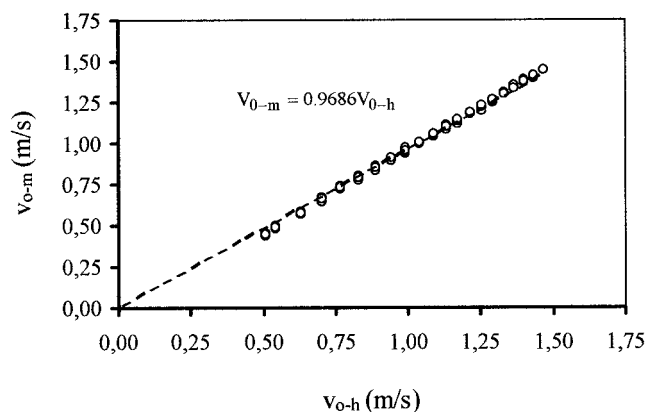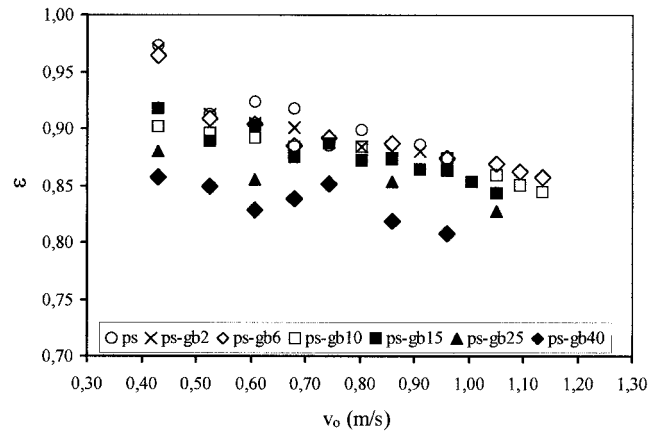

Figure 5 Impact speed calibration.
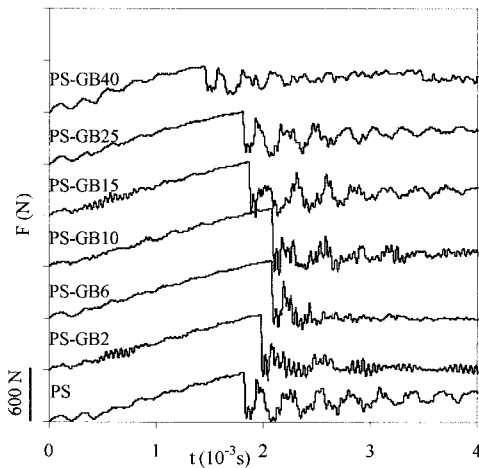
Figure 6 Force–time register for the composites tested in high-energy impact arrangement. Curves are shifted 600 N in the y-axis to examine the graphs more clearly. Impact speed = 0.82 m/s.

Figure 7 Evolution of the restitution coefficient before the drop velocity.

10%, whereas the dynamic effects were kept low. The response curve was linear up to the maximum force where fracture was produced, and then sharply decreased to zero, in accordance with the behavior of a brittle material. The oscillations superimposed in the graphs after the impact (Fig. 6) are a consequence of the slight gap between the impact point and the load gauge location. The application of impact velocities of about 1 m/s results in fully oscillating curves.

The enlargement of the initial straight part of the curve yields the Young's composite modulus, whereas the stress at break was determined from the maximum force peak. The results are detailed in Table II. The modulus increases, whereas the break stress reaches a maximum and then decreases slowly as more beads are added to the composites. The modulus increment is logically derived from the growth in rigidity given by the second phase. On the other hand, the decrease in the break stress is a consequence of the stress concentration factor and follows a tendency similar to that predicted by common models for reinforced particles.[14]

TABLE II
Stresses and Energy Results Obtained at High-Energy Impact Testing

Sample	High-energy impact		
	E_{HE} (MPa)	σ_{break} (MPa)	U_{HE} (J)
PS	3388 ± 139	67.3 ± 3.1	0.37 ± 0.05
PS–GB2	3262 ± 104	68.5 ± 0.8	0.43 ± 0.05
PS–GB6	3372 ± 35	73.0 ± 1.7	0.47 ± 0.03
PS–GB10	3356 ± 98	71.3 ± 2.8	0.47 ± 0.04
PS–GB15	3342 ± 70	68.7 ± 2.8	0.45 ± 0.04
PS–GB25	3619 ± 288	65.3 ± 3.7	0.33 ± 0.03
PS–GB40	3912 ± 145	57.4 ± 2.4	0.27 ± 0.02

The energy absorbed by the sample was calculated indirectly through the kinetic energy lost by the dart. In Table II it can be observed how the energetic level (U_{HE}) increases up to middle glass bead content, where the dissipation mechanisms, mainly crazing and particle detaching, are very efficient. This situation is identical to that observed at low velocity in traction and at impact velocity on Charpy configuration,[15] where only a limited quantity of particles was needed to produce the maximum toughening effect. When the glass spheres are very close, the propagating crack does not interact and the efficiency of glass beads as toughening agent decreases dramatically. In falling weight impact testing the same trends are observed, although the differences between composites are small.

Low-energy impact testing

Restitution coefficient

The evolution of the composites' restitution coefficient (ϵ) vs. the drop velocity is represented in Figure 7. From the experimental data it can be observed that the coefficient is velocity dependent and tends to diminish as the velocity increases. In other parallel experiences over HIPS and HIPS/PS blends, the coefficient was also found to be dependent on the falling mass and on the striker radius.[26]

The medium variation range of the restitution coefficient for the whole composite series was found to be about 0.16 units, ranging from a maximum of 0.97 for net PS to a minimum of 0.81 for PS–GB40. With respect to the impact speed, the shift inside any composition is about 0.05 units. In absolute terms, these ranges of variation are quite small, although its importance grows when the high rigidity and low specimen deformation are taken into consideration. The restitution coefficient is found to be more sensitive to changes

TABLE III
Representative Values for the Series Damped Model

ζ	$\sqrt{1 - \zeta^2}$	ε	$\varepsilon^{t_{F_m}}/t_c$	$\dfrac{1/\sqrt{1 - \zeta^2}}{\sin W_d t_{F_m}}$	t_{F_m}/t_c
0.05	0.998	0.854	0.927	1.00	0.484
0.08	0.997	0.777	0.887	1.00	0.474
0.11	0.994	0.706	0.851	1.00	0.465
0.14	0.990	0.641	0.817	1.00	0.455
0.17	0.985	0.582	0.785	1.00	0.445
0.2	0.980	0.527	0.756	1.00	0.436
0.23	0.973	0.476	0.729	1.00	0.426

affecting the rigidity that those affecting the impact velocity, which is reasonable with regard to the low composite viscoelasticity.

As can be expected, the composites containing glass beads exhibit a lower restitution coefficient compared with that of net PS because of the rigidity increment impaired by the microspheres. This fact can be observed mainly in PS–GB25 and PS–GB40 cases. The ϵ–v_0 slope reaches a value around 0.08 for all compositions, suggesting a homogeneous variation of the restitution coefficient with the impact speed.

In spite of the low variation of the restitution coefficient, these sets of results confirm that the general hypothesis of neglecting the energy losses in impact events is not completely right and the conservative model is inaccurate, even for very elastic and brittle polymers.

Nonconservative model analysis

The expression of the force predicted by the nonconservative model [eq. (25)] was split into three terms. The relative importance of each one can be studied as a function of the damping coefficient ζ. The values of the expression that correlates w_n and w_d [eq. (16)], the values of second and third terms of eq. (25), and the ϵ values are collected in Table III as a function of ζ.

It can be observed that, whatever the value between 0.5 and 1, w_n and w_d are equal, given that the value of the square-root term (second column of Table III) is almost one. Moreover, the third term of eq. (25) (fifth column of Table III) is always equal to one in the considered range. As a result, the expression for the maximum force could be simplified, obtaining the following form:

$$F_m = m v_0 w_n \varepsilon^{t_{F_m}/t_c} \qquad (27)$$

According to the above expression the maximum force is similar to that of the conservative model, but affected by the restitution coefficient, whose index value t_{F_m}/t_c is close to 0.5. The force–time trace will diverge from the semisinusoidal curve as the value of the restitution coefficient decreases.

If we now consider the contact time, it follows that

$$w_n = \frac{\pi}{t_c} = \sqrt{\frac{K}{m}} \qquad (28)$$

and

$$t_c = \pi \sqrt{\frac{m}{K}} \qquad (29)$$

This last expression implies that the contact time is not a function of the restitution coefficient, but depends on the dropping mass and the specimen compliance. The dropping mass was kept invariable during all the essays, so the contact time will vary only when a change in the specimen—attributed to plasticity, flaw, break, or other any circumstance—changes the sample compliance; in other cases, the contact time will remain unchanged.

If we apply to eqs. (27) and (29) the boundary condition imposed by the simple supported arrangement, the contact time equation is, finally,

$$t_c h^{3/2} = \frac{\pi \sqrt{m}}{\sqrt{\dfrac{4\pi E}{3r^2(3 + \nu)(1 - \nu)}}} \qquad (30)$$

and for the maximum force we have

$$\frac{F_m}{h^{3/2}\varepsilon^{t_{F_m}/t_c}} = m^{1/2}\sqrt{\frac{4\pi E}{3a^2(3 + \nu)(1 - \nu)}}\,v_0 \qquad (31)$$

In the first equation the Young's modulus is directly obtained by means of the contact time. From the second equation the slope of the representation of the left term versus v_0 will give the Young's modulus.

Application of low-energy impact testing to PS–GB composites

The progressive increment of the impact energy caused different superficial and microstructural changes in the composites that were detected after inspection of the damage zone. The change patterns were as follows: at very low impact velocities there were no signal of damage and the composites behaved in a linear elastic way. A slight increment in the impact energy causes the appearance of the initial damage that was revealed in the form of either crazing or sample shadowing. Finally, higher levels of the impact energy caused the samples to break up. The onset velocities at which the mentioned damage was detected are represented in the plot of the normalized contact time vs. the drop velocity [Fig. 8(a)].

If we focus on the representation of Figure 8(a), two different material behaviors can be clearly distinguished. The first is represented by a group of exper-

(a) **(b)**
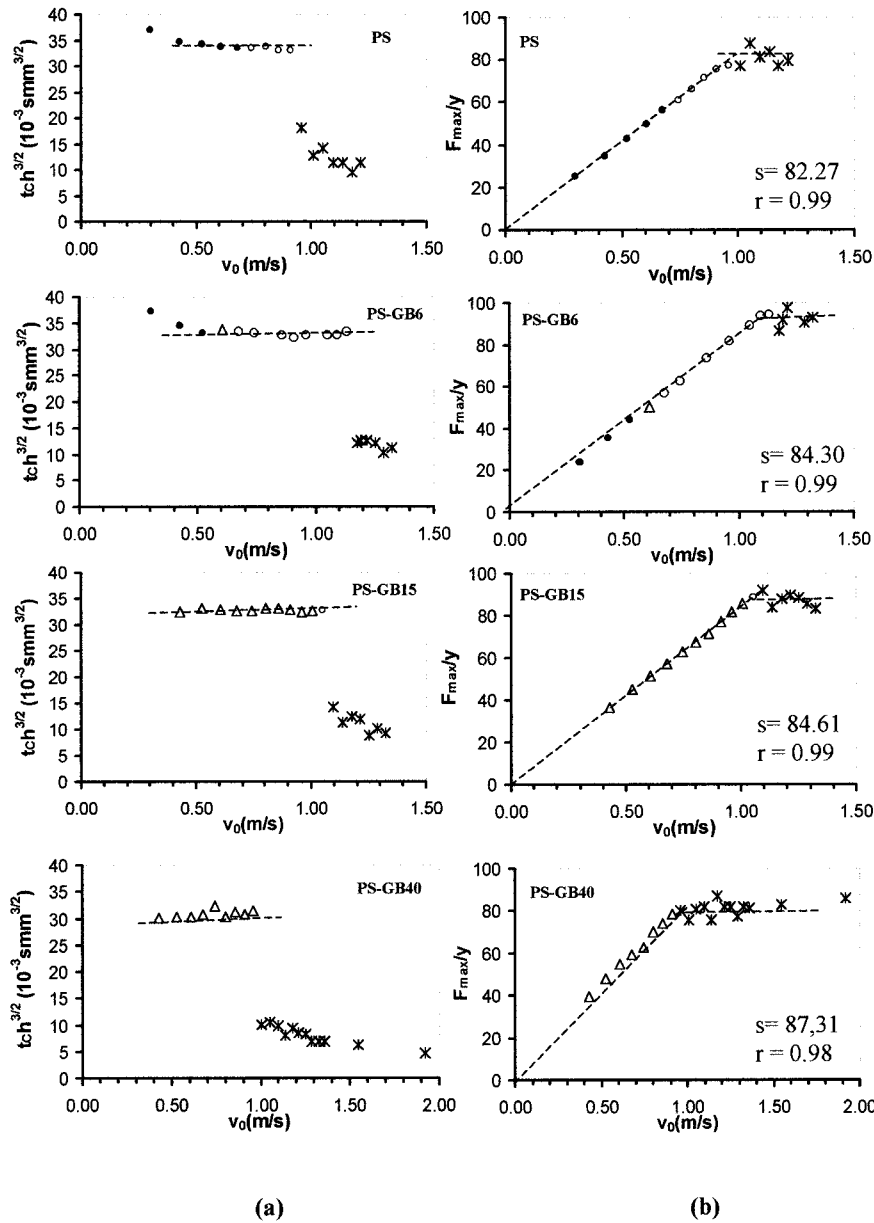
Figure 8 (a) Plot of normalized force versus corrected impact velocity; (b) plot of normalized contact time vs. impact velocity. Legend of left vertical axis: $y = h^{3/2}m^{1/2}\epsilon^{t_{Fm}/t_c}$ units are N mm$^{-3/2}$ kg$^{-1/2}$. Dotted lines are included as a guide. s, slope; r, regression coefficient. Symbols legend: ●, no damage; ○, crazing; △, shadowing; *, break.

imental points located in the low velocity range. This group of points is characterized by no damage, crazing, or shadowing, and have higher contact time values. The second group of points is located at high impact velocities and belongs to the specimens that undergo fracture. This group of points has the lower contact time values.

In the nondamaged samples, because ϵ was almost unity, the contact time was constant and approximately double the time to reach the maximum force. This provides evidence of a central symmetry with regard to the maximum force point, which is typical of a semisinusoidal curve and corroborates

that the model well represents the initial lineal-elastic behavior of the tested materials. The samples that undergo crazing seem to have a slightly lower contact time value, although the differences with the rest of experimental points are very small and not significant.

For the broken samples the contact time suddenly decreases to a very small value, which is a consequence of the abrupt change in the material rigidity attributed to the appearance of flaws or sample rupture. The limit point defines the maximum stress that the composite can withstand. Beyond this point the model does not apply.
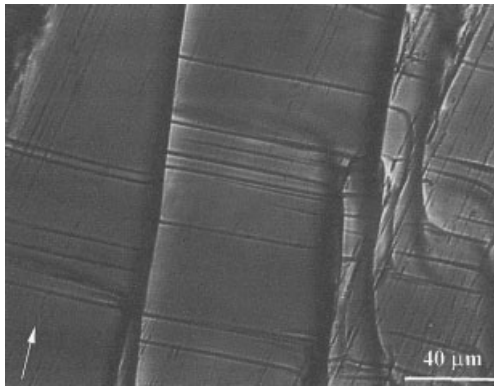
Figure 9 Top surface observation of the impacted zone in PS sample showing crazing bands. Arrow indicates the preferential direction of melt during injection molding. Small and discontinuous inclined traces are superficial grates.

The damped model predicts the force to grow linearly as the velocity or the drop height is increased [eq. (31)]. The plot of the normalized force versus corrected drop velocity follows the aforementioned rule, giving straight lines that initiate at the origin. The graphs are very linear until high velocities are reached; at this moment, the presence of internal cracks or fractures changes the sample rigidity and the experimental points diverge from the adjusted lines [Fig. 8(b)].

When the amount of glass beads is either negligible or very low, only the crazing phenomenon is observed to appear before breakup of the specimen. No variation in the slope of the adjusting line is observed. The explanation of this behavior could be that, because crazing appears in a small zone near the contact point, it presumes a very low amount of absorbed energy. In the second term, the crazes are formed by highly drawn material bridging an internal void. As a result, the whole material would be capable of supporting greater efforts than those just necessary to cause crazing to appear. The change in rigidity by the appearance of crazing is not noticeable from the force graphs, so, in this sense, the contact time is more sensitive.

The microscopic observation of the back surface of PS at the impacted region (Fig. 9) reveals an inelastic matrix deformation in the form of crazing bands. The bands are sharply defined and appear as a set of brilliant and filamentous folds. On the other hand, the bands seem to be oriented following the main injection direction and its perpendicular, a phenomenon that can be explained by a residual molecular orientation resulting from the injection molding that remains even after sample conditioning. When glass beads are added to the neat resin, the orientation is not enhanced. The glass spheres promote the sample isotropy, thus tending to smooth the residual orientation.

As the amount of glass beads is increased (PS–GB6/PS–GB10), the impacted zone shadows. The glass beads used were nontreated and thus this phenomenon is attributed to the matrix-spheres detaching and to the formation of voids near the poles.[12,27] In the most highly filled samples (PS–GB15 to PS–GB40) the shadowing increases because more spheres detach, thus hindering the observation of crazing at the back zone. If the falling energy is increased the matrix finally breaks through cracks that originate preferably from detached particles, as can be seen in Figure 10.

Once the impact energy reaches a level high enough to cause the sample to break up, the maximum force oscillates around a critical level. This level marks the threshold force or stress necessary to just produce a catastrophic crack in the studied material.

In Figure 11 there are represented the transversal fracture surfaces under the impacted zone for two composites containing 10 and 25% of glass beads. In both microphotographs, a deformed zone located at the vicinity of the impacted area could be ascertained. In low-filled samples, as in PS–GB10, it can be observed that before fracture, the material was locally compacted by the impact making up a hemispherical cap shape. Although some internal defects in the form of small cracks may appear in the impacted area, these
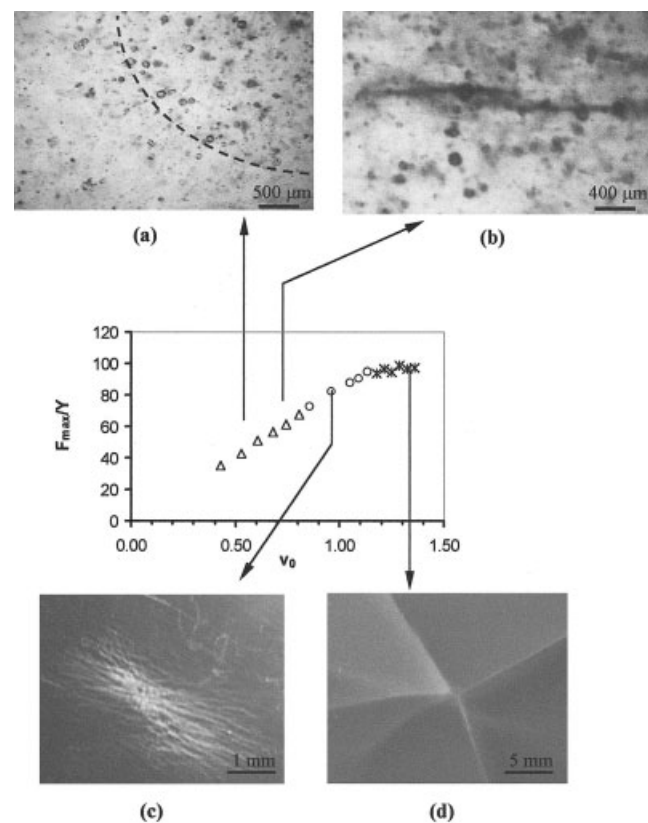
Figure 10 General events observed of the composites during impact. PS–GB10 sample: (a) Shadowing by detached particles (dotted area indicates the impact area); (b) crack growing from a detached particle (shadowing is increased); (c) crazing; (d) sample rupture.
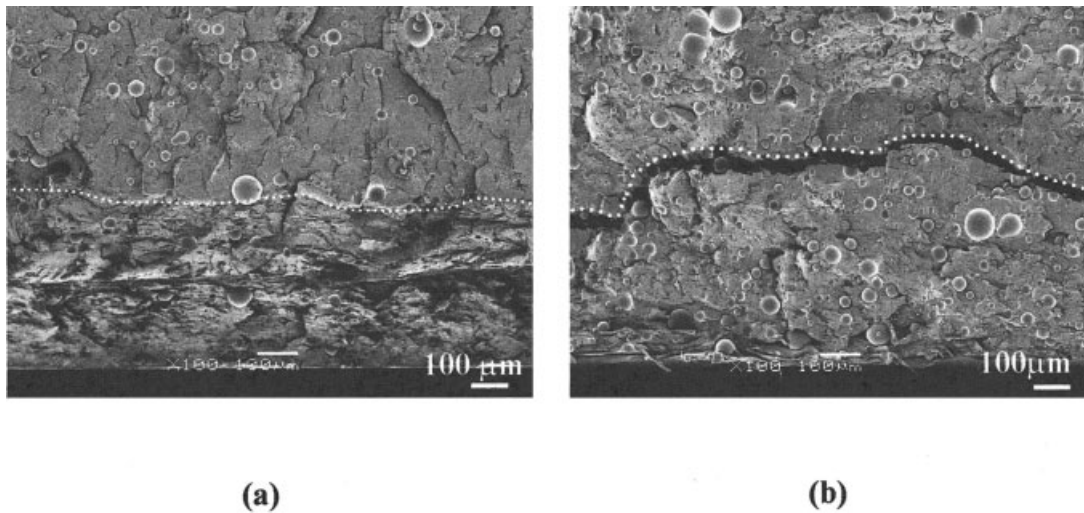
Figure 11 Scanning micrographs of the fracture surfaces of composites after low-energy impact. (a) PS–GB10 after shadowing; (b) PS–GB25 after shadowing near the breaking point. The impacted zone is at the bottom of the micrographs. The white dotted line defines the limits of the process zone.

cracks seems not to propagate because the same material can support higher impact loadings before undergoing a complete fracture. When both the load and the amount of glass beads are increased, as in PS–GB25 sample [Fig. 11(b)] or in PS–GB40 sample (Fig. 12), the deformed zone changes and instead of compacting, a transversal crack surrounding the contact area appears. If we consider the whole fracture surface after the impact, as shown in Figure 12, it can be ascertained that the origin of the failure occurs at the bottom side of the specimen, that is, the side away from the impact point. This side of the sample is in a tensile state of stress and therefore will fail before the upper part of the specimen. Once started, the failure crack advances across the specimen thickness in the

transversal direction and mainly toward the contact point. It is probably at this moment when the contact damage zone splits from the rest of the sample when the fast propagating crack approaches it.

If the evolution of the maximum force, or stress, vs. the amount of glass beads is considered, it can be found that the threshold stress initially increases, as far as a peak is reached, around a glass content of 10%. A further increment in the glass content causes the stress to progressively slow down (Table IV). This situation is similar for the absorbed energy with a maximum in the low range of glass beads content.

It is well known that rigid particles can toughen by interactions with a propagating crack, pinning the crack front or bowing it.[28] Working with glass bead–filled epoxies, Norman[13] recently pointed out that the main toughening mechanism is attributed to off-fracture plane processes of particle–matrix detaching and by the following inelastic matrix deformation around the particles. These mechanisms seem to be acting here too, as can be observed in Figures 10 and 11. Table IV also presents the values of the whitening or detaching onset stresses and, for the samples where it was possible to be observed, the crazing stress. The appearance of shadowing is produced almost at constant stress and independent of the glass bead amount, having a value of 18.8 MPa. The stress to initiate crazing is around 40 MPa, and 44.4 MPa for the net polystyrene.

For the nonconservative model the Young's moduli were calculated from eqs. (30) and (31) and are collected in Table IV. It can be observed that, in the range of experimental error, almost identical values are obtained independent of the procedure by maximum force or contact time. The contact time method seems
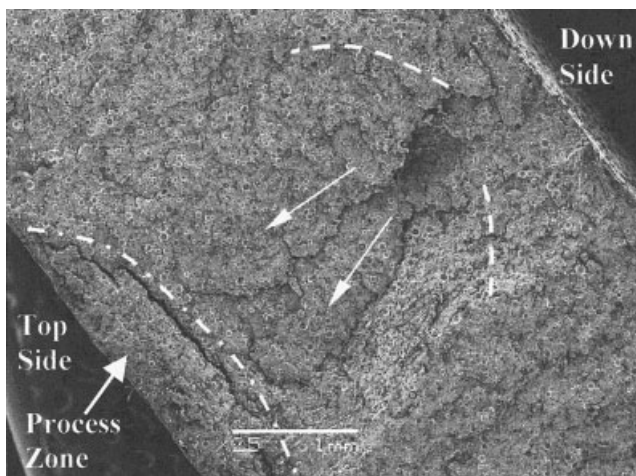
Figure 12 Scanning micrograph of the whole surface fracture after low-energy impact over the PS–GB40 sample. Arrows indicate the crack-propagation direction.

TABLE IV
Modulus and Stresses Results Obtained at Low Energy Impact Testing[a]

Sample	Low-energy impact				
	$E_{F_{max}}$ (MPa)	E_{t_c} (MPa)	σ_{shadow} (MPa)	σ_{craze} (MPa)	σ_{break} (MPa)
PS	3283 (0.998)	3151 ± 100	—	44.4	55.2 ± 2.4
PS–GB2	3336 (0.997)	3218 ± 118	—	39.8	64.8 ± 3.4
PS–GB6	3460 (0.998)	3287 ± 122	—	39.7	66.6 ± 3.7
PS–GB10	3415 (0.997)	3241 ± 140	18.2	50.4	67.7 ± 2.9
PS–GB15	3513 (0.990)	3321 ± 57	18.6	—	62.4 ± 2.2
PS–GB25	3558 (0.987)	3533 ± 83	18.9	—	60.4 ± 1.6
PS–GB40	3792 (0.983)	3870 ± 190	19.4	—	54.4 ± 2.3

[a] The regression coefficient is in parentheses. Results with no standard deviation are onset values.

the most sensitive to physical variations that could be developed in the specimens; on the other hand, the modulus derived from the registered force is not influenced by graphs peaks, given that the oscillations around maximum force are negligible.

For a given PS–GB composite, the modulus derived either from low-energy configuration or from high impact energy configuration results in quite similar values. Slight differences arise when accounting for the impact velocity of both methods. However, considering the stiffness of the tested material, no great variations are expected by sample viscoelasticity in the range of speeds selected. In any case, the results obtained from the high-energy arrangement seem to overestimate the Young's modulus and are subjected to a major experimental variation.

CONCLUSIONS

Two alternative methods have been proposed to easily calculate the restitution coefficient using the falling weight impact technique. The first method is based on the noncontact time, whereas the second uses the integration of the first force–time trace. A simple nonconservative series model with analytical solution can be successfully applied to determine the mechanical sample properties at high strain rates.

The low-energy impact method is appropriated to follow the damage phenomena that occur in the samples. The contact time seems to be more sensitive to slight variations in the sample rigidity; however, the procedure through use of the maximum force gives more reliable results. The applications of both methods to PS–GB samples result in similar mechanical values that are in agreement with the expected behavior for this kind of materials.

The application of high-energy impacts over the PS–GB composites results in oscillating but straight curves up to the break point. The values of the elastic modulus obtained from this arrangement are slightly overestimated, especially in the more highly filled samples, as consequence of the major contribution of dynamic effects. Under moderated strain rates, con-

centrations of glass beads equal to or lower than 15% in weight have only a slight reinforced effect, whereas contents above 15% in weight facilitate the failure. The failure mechanism initiates with beads detaching, followed by a crack or craze that is formed preferentially in the vicinity of the previous detached particle. A splitting crack seems to originate at the bottom side of the specimens under a tensile state of stress.

The nonconservative model that is proposed, in spite of the improvements regarding the conservative one, does not fully represent the whole impact behavior because indentation effects are not taken into account.

References

1. ISO 6603-2:2000, Plastics. Determination of Puncture Impact Behaviour of Rigid Plastics, Part 2: Instrumented Puncture Test; European Committee for Standardisation (2000).
2. Pavan, A. In: Fracture Mechanics Testing Methods for Polymers Adhesives and Composites, ESIS Publication 28; Moore, D. R., Pavan, A., Williams, J. G., Eds.; Elsevier Science: Amsterdam, 2001; pp 27–58.
3. Fasce, L. A.; Pettarin, V.; Seltzer, R.; Frontini, P. M. Polym Eng Sci 2003, 43, 1081.
4. Chivers, R. A.; Moore, D. R. Polym Technol 1990, 1, 313.
5. Karger-Kocsis, J.; Mouzakis, D. E.; Ehresnstein, G. W.; Varga, J. J. J Appl Polym Sci 1999, 73, 1205.
6. Ramsteiner, F. Polym Test 1999, 18, 641.
7. Tai, C. M.; Li, R. K. Y.; Ng, C. N. Polym Test 2000, 19, 143.
8. Sutherland, L. S.; Guedes Soares, C. Compos Sci Technol 2003, 63, 1.
9. Rodríguez-Pérez, M. A.; Velasco, J. I.; Arencón, D.; Almanza, O.; De Saja, J. A. J Appl Polym Sci 2000, 75, 156.
10. Casiraghi, T.; Castiglioni, G.; Ronchetti, T. J Mater Sci 1988, 23, 459.
11. Williams, J. G.; Adams, G. C. Int J Fract 1987, 33, 209.
12. Vollenberg, P.; Heikens, D.; Ladan, H. C. B. Polym Compos 1988, 9, 382.
13. Norman, D. A.; Robertson, R. E. Polymer 2003, 44, 2351.
14. Nielsen, L. E.; Landel, R. F. Mechanical Properties of Polymers and Composites, Vol. 2; Marcel Dekker: New York, 1994.

15. Sanchez-Soto, M.; Gordillo, A.; Maspoch, M. L. L.; Velasco, J. I.; Santana, O. O.; Martínez, A. B. Polym Bull 2002, 47, 587.

16. Johnson, K. L. Contact Mechanics; Cambridge University Press: Cambridge, 1985.

17. Macaulay, M. A. Introduction to Impact Engineering; Chapman & Hall: London, 1987.

18. Williams, J. G.; Rager, A. In From Charpy to Present Impact Testing, ESIS Publication 30; François, D.; Pineau, A., Eds.; Elsevier Science: Amsterdam, 2002; pp 33–44.

19. Timoshenko, S. P.; Woinowsky-Krieger, S. Theory of Plates and Shells, 2nd ed.; McGraw-Hill: Kogakusha, Tokyo, 1984.

20. Young, W. C. Roark's Formulas for Stress and Strain, 6th ed.; McGraw-Hill: Singapore, 1989.

21. Hartog, J. P. Mechanical Vibrations; Dover Publications: New York, 1985.

22. Hutchings, I. M. J Phys D Appl Phys 1979, 12, 1819.

23. Karger-Kocsis, J. Macromol Symp 1999, 143, 185.

24. Velasco, J. I.; Morhain, C.; Martínez, A. B.; Rodríguez-Pérez, M. A.; de Saja, J. A. Polymer 2002, 43, 6805.

25. Velasco, J. I.; Morhain, C.; Martínez, A. B.; Rodríguez-Pérez, M. A.; de Saja, J. A. Polymer 2002, 43, 6813.

26. Jiménez, O. Ph.D. Thesis, Universitat Politecnica de Catalunya, Terrassa, Spain, 2002.

27. Lee, J.; Yee, A. F. Polymer 2001, 42, 577.

28. Lange, F. F. In: Mechanics of Composite Materials; Jones, R. M., Ed.; Scripta Book Co.: Washington, DC, 1975.